nature materials

Article

https://doi.org/10.1038/s41563-024-01866-4

Elementary excitations of single-photon emitters in hexagonal boron nitride

Received: 13 September 2022

Accepted: 15 March 2024

Published online: 23 April 2024

Check for updates

Jonathan Pelliciari ®¹⊠, Enrique Mejia², John M. Woods², Yanhong Gu¹, Jiemin Li¹, Saroj B. Chand ®², Shiyu Fan ®¹, Kenji Watanabe ®³, Takashi Taniguchi ®⁴, Valentina Bisogni ®¹ & Gabriele Grosso ®².5⊠

Single-photon emitters serve as building blocks for many emerging concepts in quantum photonics. The recent identification of bright, tunable and stable emitters in hexagonal boron nitride (hBN) has opened the door to quantum platforms operating across the infrared to ultraviolet spectrum. Although it is widely acknowledged that defects are responsible for single-photon emitters in hBN, crucial details regarding their origin, electronic levels and orbital involvement remain unknown. Here we employ a combination of resonant inelastic X-ray scattering and photoluminescence spectroscopy in defective hBN, unveiling an elementary excitation at 285 meV that gives rise to a plethora of harmonics correlated with single-photon emitters. We discuss the importance of N π^* anti-bonding orbitals in shaping the electronic states of the emitters. The discovery of elementary excitations in hBN provides fundamental insights into quantum emission in low-dimensional materials, paving the way for future investigations in other platforms.

Hexagonal boron nitride (hBN) is a versatile material with applications in multiple scientific fields due to its properties, including air stability, hyperbolic dispersion and strong optical nonlinearities¹. It is composed of a hexagonal lattice of alternating B and N atoms (Fig. 1a) whose hybridization leads to a wide bandgap in the ultraviolet range. The discovery of single-photon emitters (SPEs) in hBN has spurred scientific interest due to their room-temperature operation², high brightness³, frequency tunability⁴, stability⁵, narrow linewidth⁶ and optically detected magnetic resonances⁷. In hBN, SPEs have been associated with defects whose electronic levels within the bandgap generate quantum light with narrow and well-defined energies (Fig. 1b) defined by the atomic composition of orbitals involved in the electronic transition. Although these aspects have been extensively studied, no consensus to an underlying mechanism for hBN emitters has been reached yet⁸⁻¹¹. The characterization of SPEs in hBN has been mostly limited to photoluminescence (PL) spectroscopy, measurements of the second-order autocorrelation function $(g^2(\tau))$ and magnetic resonances. These efforts identified the negatively charged boron vacancy (V_B^-) as a consistent defect ^{12,13}, but could not reveal the properties of all other hBN emitters ¹⁴, leaving the microscopic details necessary to explain the large distribution of the emission energies of SPEs in hBN still obscure.

By combining resonant inelastic X-ray scattering (RIXS) and PL spectroscopy, we unveil the presence of elementary electronic excitations correlated to most of the SPEs in the visible spectrum of hBN. Our RIXS measurements on defective hBN uncover an excitation at E_0 = 285 meV that propagates up to 2.3 eV through multiple regular harmonics E_n = nE_0 , where $n \in \mathbb{N}$. An independent analysis of the PL spectral emission containing multiple SPE peaks with a model that includes recombination processes similar to donor–acceptor pairs (DAP) reveals fundamental transitions matching the energy of the harmonics observed with RIXS at n = 5–8. Thus, using only a limited set of parameters, we show that the sequence of harmonics E_n based on the elementary energy E_0 can explain the wide frequency range of quantum emission in hBN.

¹National Synchrotron Light Source II, Brookhaven National Laboratory, Upton, NY, USA. ²Photonics Initiative, Advanced Science Research Center, City University of New York, New York City, NY, USA. ³Research Center for Functional Materials, National Institute for Materials Science, Tsukuba, Japan. ⁴International Center for Materials Nanoarchitectonics, National Institute for Materials Science, Tsukuba, Japan. ⁵Physics Program, Graduate Center, City University of New York, New York, NY, USA. ⊠e-mail: pelliciari@bnl.gov; ggrosso@gc.cuny.edu

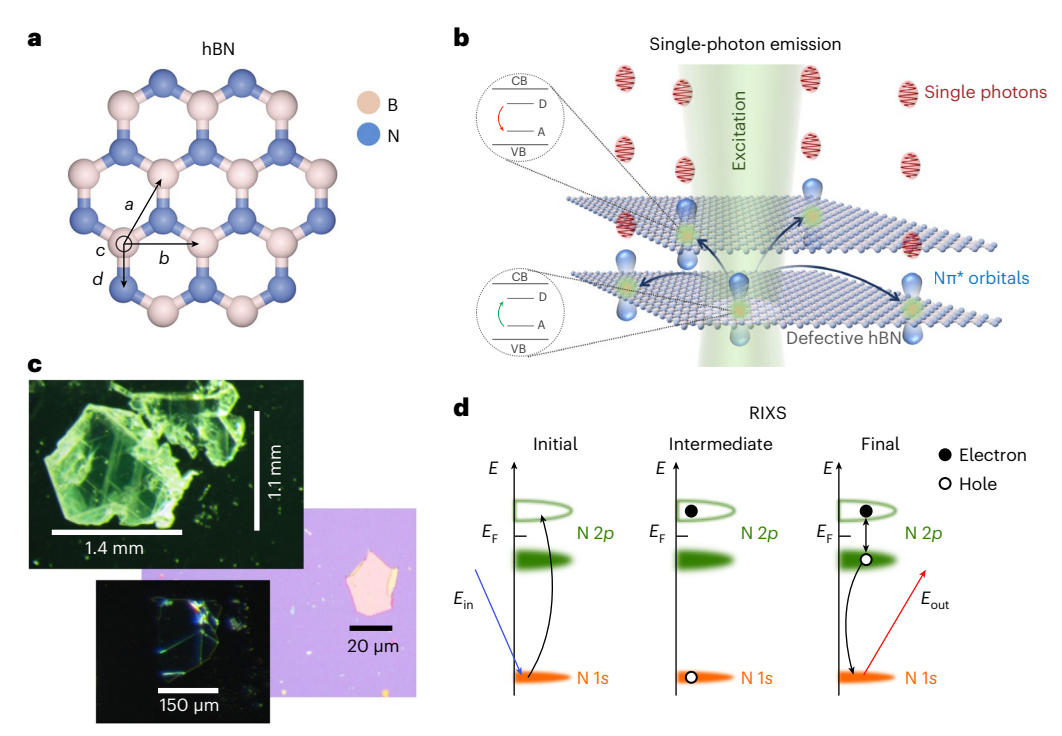


Fig. 1| **Single-photon emission and RIXS processes in hBN. a**, Crystal structure of a single layer of hBN. The lattice vector \vec{c} points out of the plane and connects two hBN layers. **b**, Single-photon emission process in layered hBN showing the delocalized recombination process involving N π^* orbitals (highlighted with the blue pair of lobes oriented vertically on opposite sides of the hBN plane). On

excitation of a donor defect, electrons can recombine with acceptors at a distance of a few atomic sites and emit single photons (depicted with red ovals). CB, conduction band; VB, valence band. \mathbf{c} , Microscopy images of hBN single crystals used for this study in bulk (top) and in thin flakes exfoliated on a Si/SiO₂ substrate (bottom). \mathbf{d} , Diagram of the generalized RIXS process at the N–K edge.

RIXS on hBN

The sensitivity of RIXS to elementary electronic excitations is given by a resonance effect in which a core electron is excited to the conduction band creating a real short-lived (a few femtoseconds) intermediate state that radiatively decays, emitting a photon and leaving the system in a neutral excited state (Fig. 1d)¹⁵. The coherence of this process allows sensitivity to all the electronic degrees of freedom, that is, spin, charge, orbital and lattice excitations 16,17. Recent technological developments have enabled the study of micrometre-sized samples (Fig. 1c) with high energy resolution ^{18–21}. At the N–K edge, the atomic transition of RIXS is $1s \rightarrow 2p/sp^2$ and $2p/sp^{2*} \rightarrow 1s$ of nitrogen (Fig. 1d). In Fig. 2a, we report the X-ray absorption spectra (XAS) at the N-K edge in σ polarization for pristine hBN of different thicknesses (bulk, 100 and 40 nm thick). The first peak at ~401.5 eV is a transition from N 1s to N π^* orbitals, whereas the peaks at higher energy are ascribed to transitions from N1s to N σ^* orbitals²²⁻²⁴. Pristine hBN samples are exfoliated flakes from high-quality bulk material with extremely low concentration of defects and no presence of SPEs or other emissions below the bandgap²⁵. Defective hBN samples are prepared by irradiating pristine flakes with argon plasma followed by high-temperature annealing (Methods). This technique has been proven to be effective in generating defect-based SPEs in hBN, with sharp emission energies spanning a large spectral range²⁶. The RIXS spectra at different incident photon energies for pristine as well as defective hBN (20 nm) are reported in Fig. 2b. The RIXS spectra display a strong diffuse scattering line at 0 eV in energy loss and multiple peaks at finite energy. Depending on the incident energy, we identify two different responses. At the N σ^* XAS resonance, RIXS probes the phonon modes for both pristine and defective hBN (Fig. 2c and Supplementary Figs. 7 and 8). The measured energies for the phonon modes agree with the Raman and inelastic X-ray scattering results for the bulk²⁷. At the N π * XAS peak, no signal is observed for pristine hBN (Fig. 2b), whereas for defective hBN, multiple harmonic peaks appear with an elementary energy of $E_0 = 285$ meV. The detection of phonons or harmonics as a function of incident photon energy is rationalized in Fig. 2d,e, where we illustrate a diagram of the molecular orbitals of hBN (Fig. 2d). In hBN, orbital hybridization leads to the formation of three σ^* anti-bonding orbitals and one π^* anti-bonding orbital, which—when excited in the RIXS process—result in phononic detection or harmonics, respectively (Fig. 2e). In Fig. 2e, we show that the energy of the harmonics does not match the one of the phonons, corroborating the different electronic sensitivities of RIXS rather than a mere rescaling of the intensity of the same peaks.

We now discuss the RIXS data from three defective hBN flakes with approximate thicknesses of 20 nm (flake 1), 100 nm (flake 2) and 200 nm (flake 3). The spectra in Fig. 3a,b are obtained by exciting at two energies around the N pre-edge π^* transition. The series of harmonic peaks spans a different energy window depending on the incident photon energy: it extends up to 1.50 and 2.30 eV when excited at 401.55 and 402.30 eV, respectively. The number of harmonics probably depends on the incident energy available to promote electrons above the Fermi level as the difference in incident energy (0.750 eV) is consistent with the energy of the highest harmonic detected (1.5 versus 2.3 eV). Reproducibility on multiple samples is impressive as plasma treatment is an aggressive and non-selective method to induce defects, indicating the robustness and generality of these harmonics in defective hBN. In Fig. 3c, we compare the first peak of the harmonic for three defective flakes, showing that in all the cases, the peak linewidth approaches the RIXS energy resolution of 20 meV (instrumental broadening; Fig. 3e). This further confirms that RIXS detects fundamental transitions in defective hBN, that their elementary energy is 285 meV and that the harmonics are invariant under plasma treatment and flake thickness.

We extract the energy, intensity and linewidth of the RIXS peaks at the N π^* resonance by fitting them with Gaussian functions (Supplementary Information provides further details). In Fig. 3d, we compare the peak intensities of defective flakes 1 and 2. In both cases, the intensity does not follow any exponential or monotonic trend, but it

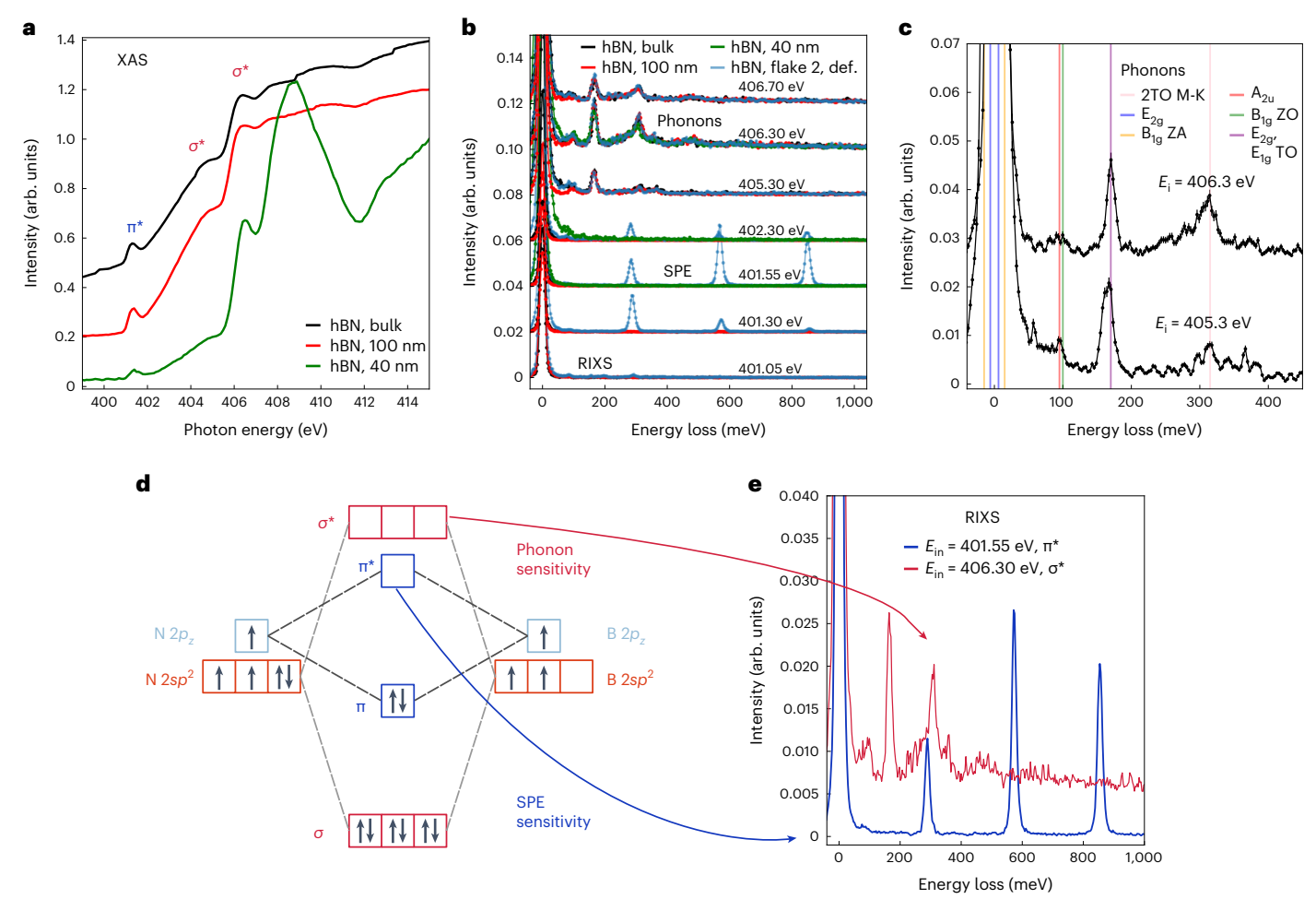


Fig. 2 | **XAS** and **RIXS** measurements on hBN. **a**, XAS data of pristine hBN as a function of thickness in σ polarization. **b**, RIXS data of pristine hBN and defective hBN as a function of thickness and incident energy. Incident polarization was set to σ . At high incident energy (main N–K edge), the RIXS signal is qualitatively different than at the pre-edge. **c**, Zoomed-in view of the RIXS spectrum of an hBN crystal, showing the sensitivity of RIXS to phonons. The energy of the main phonon modes extracted from inelastic X-ray scattering and Raman studies 27

are highlighted with vertical lines. \mathbf{d} , \mathbf{e} , Molecular orbital diagram of hBN (\mathbf{d}) that illustrates the connection between incident excitation energy and sensitivity of RIXS to phonons or SPEs (\mathbf{e}). The diagram assumes the same energy for N 2 sp^2 /B 2 sp^2 and N 2 p_z /B 2 p_z orbitals. The error bars of the RIXS intensity in \mathbf{b} , \mathbf{c} and \mathbf{e} are the square root of the total number of photons (n > 20) detected on the RIXS detector before normalization. When the error bars are not visible, they are smaller than the marker size.

has a maximum at n = 2 when excited at $E_{in} = 401.55$ eV, whereas for $E_{\rm in}$ = 402.3 eV, the trend seems to initially decrease and then increase again for n = 7 and n = 8. Previous theoretical works indicate that an exponential or monotonic decay is expected when electron-phonon coupling drives phonon detection in RIXS on solid-state materials $^{16,28-31}$. The non-exponential and non-monotonic trend observed in hBN suggests that these harmonics have a non-trivial electronic nature whose full understanding requires further dedicated studies. Similar non-exponential and non-monotonic trends have been reported for RIXS at the N π^* resonance in N₂ molecules, and have been associated with the vibrational excitation of the ground state of N_2 (refs. 32,33). Furthermore, the energies of the harmonics exhibit an almost linear trend for all the defective samples (Fig. 4a and Table 1), indicating a common intrinsic nature. There are multiple possible origins for the coherent modes emerging in defective hBN samples, but a large fraction of excitations can be ruled out by arguments based on the RIXS cross section, comparison with other solid-state systems and previous literature. Single-spin excitations are excluded as they cannot be observed at the K edges because of the lack of spin-orbit coupling of the 1s core electrons³⁴. Multi-spin excitations can also be discarded as the number of harmonics (up to ten) is inconsistent with the spin state of nitrogen. There are also reports of hybridized dd excitations coupled to phonons, but no harmonics were observed. We also exclude optical orbitons because we are not aware of any observations of excitons displaying a series of harmonics extending as high as the ones emerging in hBN 35,36. Moreover, excitons in hBN appear at an energy comparable with the bandgap, and are not compatible with an elementary energy at 285 meV. Excitations connected with the Kekulé structure (such as Kekulé bond-order excitations) of hBN can also be excluded as they should be present in pristine hBN. Therefore, the origin of harmonics should be researched in the defective structures that give rise to quantum emission.

PL spectroscopy on defective hBN

To deepen our understanding of defective hBN, we compare the RIXS data with the results from PL experiments. First, we note that a vast amount of literature shows that SPEs are commonly found at around 580 nm (2.138 eV) and 640 nm (1.937 eV) (refs. 4,14,26,37–39), with a striking match to the seventh and eighth peaks of the harmonics in the RIXS data. Moreover, SPEs have been observed at other energies reached by the harmonics, including the ones in the near-infrared (1.25 eV) (ref. 40) and the ultraviolet (2.80 eV) (ref. 5). Figure 4b shows the PL emission spectra of a plasma-treated defective sample at 8 K obtained by laser excitation at different energies (Methods and

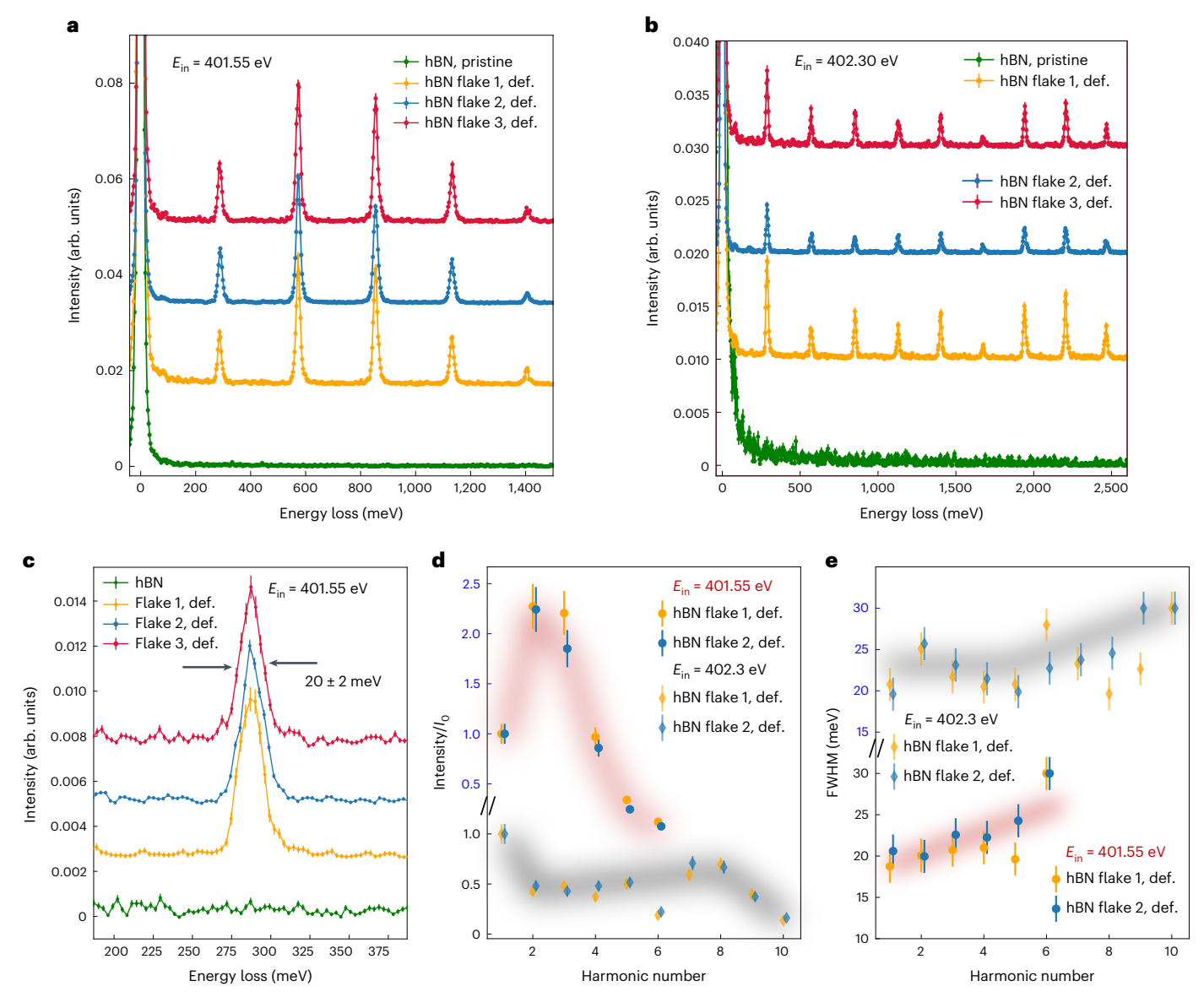


Fig. 3 | **Fundamental excitations in defective flakes of hBN. a,b,** RIXS on thin pristine hBN and defective flakes at $E_{\rm in}$ of 401.55 eV (a) and 402.3 eV (b). c, Zoomed-in views of the fundamental harmonics of defective hBN. The linewidth of the peak is comparable with the experimental resolution, indicating that the peaks are extremely narrow in energy. d,e, Results of the Gaussian fit of the peaks as a function of harmonic index on defective flakes 1 and 2. In d, we report the intensity profile normalized by the intensity of the fundamental peak, indicating a non-trivial dependence and strong oscillator strength. In e, we summarize the FWHM of the peaks as a function of harmonic number. The FWHM

changes marginally over a wide range of energy losses spanning from the infrared up to ultraviolet. The black and grey shades are guides for the eye to highlight the trend. The error bars of the RIXS intensity in \mathbf{a} - \mathbf{c} are the square root of the total number of photons (n > 20) detected on the RIXS detector before normalization. When the error bars are not visible, they are smaller than the marker size. The error bars in \mathbf{d} are based on an evaluation of the error associated with the fitting and errors due to normalization. The error bars in \mathbf{e} are based on the error (standard deviation) on the fitting.

Supplementary Information). We use different laser excitation energies to mitigate the dependence of SPEs on the incident energy and to access as many peaks as possible 41,42 . The quantum nature of the emission is confirmed by second-order autocorrelation function measurements (Fig. 4b, inset). The PL emission spectra from defective hBN (Fig. 4b) cannot be explained by only the harmonics E_n even considering the energy shifts due to strain or electromagnetic variations (in the order of 65 meV (refs. 4,43) and 15 meV (ref. 44), respectively). Further recombination mechanisms due to the incoherent nature of the PL decay process have, therefore, to be considered to account for the large spectral span of the PL emission from SPEs in defective hBN. Consequently, to compare the results of the coherent excitations of RIXS with the SPEs in PL experiments, we use a phenomenological model similar to the DAP recombination process that has been used to understand PL in

many defective semiconductor materials and hBN (refs. 45,46). A DAP process occurs when an electron from a donor defect recombines with an acceptor defect that can be at a distance of several atomic sites (Fig. 1b). A single DAP recombination generates a PL emission peak with energy $E_{\rm DA} + \frac{e^2}{4\pi\epsilon R'}$, where R is the spatial separation between the donor and acceptor site; $\epsilon = \epsilon_0 \epsilon_{\rm hBN}$ is the in-plane, bulk dielectric constant⁴⁷; and $E_{\rm DA}$ is the energy difference between the energetic levels of the donor and acceptor defects. In the presence of several defects, recombinations can occur among donors and acceptors at different sites of the lattice, and the DAP process generates a sequence of emission peaks following the discrete series:

$$\left\{ E_{\mathrm{DA}} + \frac{e^2}{4\pi\epsilon R_m}, \quad m \in \mathbb{N} \right\},\tag{1}$$

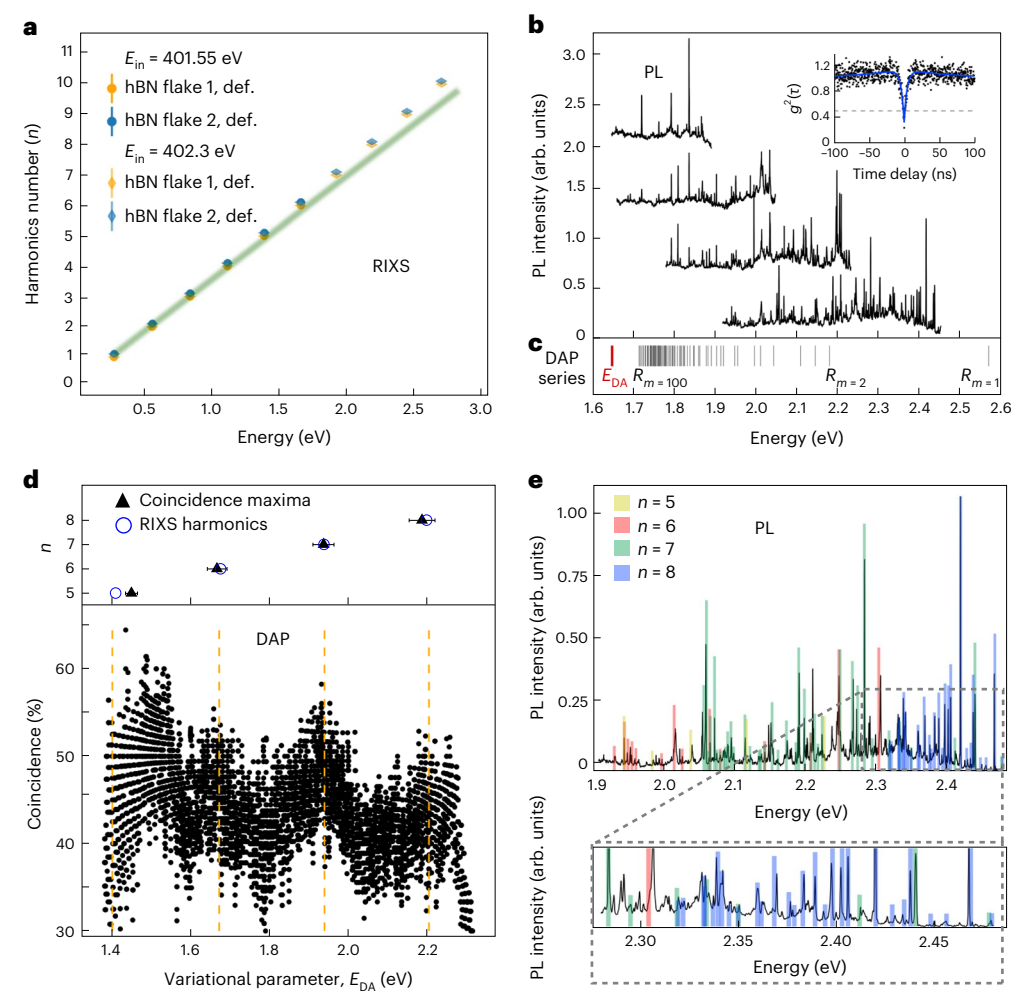


Fig. 4 | **Fundamental energies in RIXS and PL experiments. a**, Dots indicate the energy of the harmonic peaks for two defective flakes at two incident energies. The error bars of the RIXS peak energies are established on the basis of the standard deviation of fitting, resolution and estimation of the elastic line position. **b**, Emission spectra of PL experiments at 8 K recorded in the same position of a defective sample with different excitation energies ($E_{\rm exc}$) and detection ranges ($E_{\rm det}$): $E_{\rm exc} = 2.70$ eV and $E_{\rm det} < 2.48$ eV, $E_{\rm exc} = 2.43$ eV and $E_{\rm det} < 2.25$ eV, $E_{\rm exc} = 2.21$ eV and $E_{\rm det} < 2.07$ eV, $E_{\rm exc} = 2.03$ eV and $E_{\rm det} < 1.91$ eV. For clarity, the spectra are displayed with a vertical offset. The inset is an example of a second-order autocorrelation function ($g^{(2)}(\tau)$) for a single line of the spectrum. **c**, Example of a DAP series ($\{E_m\}$) for $E_{\rm DA} = 1.65$ eV up to $R_{m=100}$. **d**, Coincidences

between the SPE peaks in \mathbf{b} and the DAP series calculated with equation (1) by varying E_{DA} . Fundamental transitions E_{DA}^i maximize the coincidence counts and minimize the fit error (Supplementary Information). The top panel shows the values of E_{DA}^i resulting from the DAP fitting versus the harmonic index of RIXS. The error bars correspond to the standard deviation of the fit. The dashed orange vertical lines indicate the energy of the harmonics measured with RIXS for n=5,6,7,8. \mathbf{e} , PL spectrum for $E_{\mathrm{exc}}=2.70$ eV overlaid to the matching lines (coloured bars) of the DAP sequences from equation (2). The width of the coloured bars indicate a matching tolerance of 2 meV, whereas the height does not have physical meaning and it is chosen to resemble the intensity of the corresponding peaks.

where m is the index over all the possible distances of lattice sites (R_m) . To account for the layered structure of hBN, we include all the possible distances among lattice sites across two adjacent hBN layers, with $R_m = \{|\vec{l} \cdot \vec{d} + |\vec{b} + k\vec{c} + l \cdot \vec{d}|, i, j \in \mathbb{Z} \text{ and } k, l = 0, 1\}$ where $\vec{a}, \vec{b}, \vec{c}$ and \vec{d} are the lattice vectors (Fig. 1a). An example of a DAP series in hBN for $E_{\mathrm{DA}} = 1.65$ eV is displayed in Fig. 4c. To analyse the PL emission of defective hBN, we compare the peak energies of the PL data shown in Fig. 4b with the energy series of equation (1) generated by varying E_{DA} . We look for fundamental DAP transitions (E_{DA}^i) by estimating the number of peaks in the DAP series that match with the peaks in our data (coincidence counts) and evaluating the total energy difference between the DAP peak sequence and the experimental PL values. The fit error is calculated from the total energy difference using the least squares method (Supplementary Information provides a description of the procedure). Figure 4d reports the coincidence counts as a function of the variational parameter E_{DA} . The DAP analysis reveals the presence of four fundamental transitions E_{DA}^i characterized by the maxima of

coincidence counts. These four peaks indicate that the system can host several donor–acceptor-like transitions whose energies (E_{DA}^{i}) are in excellent agreement with previous PL experiments on hBN samples of different origins 46. The values of E_{DA}^{i} exhibit a periodic energy spacing with a linear trend (Fig. 4d, top), and a notable match with the fifth, sixth, seventh and eighth harmonics observed in the RIXS data. The linear trend, comparable energy values and regular spacing (-285 meV) of E_{DA}^{i} infer a correlation between the RIXS harmonic states (E_{n}) and SPEs. The results of the DAP analysis of the PL spectra from different samples (Supplementary Information) returns a common trend. The reliability of our DAP analysis is confirmed by a number of tests run on randomly simulated PL spectra and with synthetic DAP sequences (Supplementary Information). A confidence interval for the values of fundamental resonances E_{DA}^{i} is provided by the fit error calculated from the total energy detuning between the ideal DAP sequence and PL data. In Table 1, we compare the results of RIXS and PL experiments together with values extracted from the literature in which a

Table 1 | Comparison between energy values in RIXS and PL

Energy (in eV) of fundamental transitions as detected by different methods			
n	RIXS def.	PL	Other works
1	0.285±0.002		
2	0.572±0.002		
3	0.851±0.002		
4	1.129±0.002		1.240 (ref. 40)
5	1.403±0.002	1.444±0.010	1.430 (ref. 46)
6	1.674±0.002	1.665±0.024	1.708 (ref. 46), 1.759 (ref. 38)
7	1.941±0.002	1.940±0.026	1.950 (ref. 46), 1.938 (ref. 37), 2.033 (ref. 38)
8	2.206±0.002	2.194±0.032	2.180 (ref. 46), 2.120 (ref. 37), 2.131 (ref. 38), 2.138 (ref. 39)
9	2.467±0.002		2.411 (ref. 46)
10	2.722±0.002		2.847 (ref. 5)

This table compares the energy of the harmonics measured with RIXS, of the fundamental transitions extracted from the DAP model applied to PL spectra and of the values of zero-phonon line (ZPL) for SPEs in hBN reported in previous works in which large ensembles of emitters have been investigated. The error in the evaluation of the RIXS energies is based on an analysis of the fitting uncertainty, energy resolution and identification of the elastic line. The energies extracted from the DAP analysis of the PL data are the average between the values obtained from the curves of the coincidence and the fit error (Fig. 4c). The PL error is the error of the fit.

statistically substantial number of zero-phonon line (ZPL) transitions for SPEs in hBN are considered.

Having proved a periodic energy scale in the PL data, we now formulate an SPE series combining the RIXS harmonics and DAP model:

$$E_{\text{SPE}} = \left\{ E_{\text{DA}}^i + \frac{e^2}{4\pi\epsilon R_m} \right\}_{i,m} = \left\{ nE_0 + \frac{e^2}{4\pi\epsilon R_m} \right\}_{n,m},\tag{2}$$

where the energies of the harmonics $(E_n = nE_0)$ play the role of the energy of the donor-acceptor transitions E_{DA} of equation (1). We note that equation (2) represents a pure phenomenological description of the emission pattern in defective hBN that does not take into account the nature of the donor and acceptor states, as well as the associated absorption process. In Fig. 4e, we show that the series calculated with equation (2) can account for over 75% of the peaks observed in a PL spectrum of defective hBN. In this figure, we overlaid the lines of equation (2) onto a PL spectrum for finding a match with the experimental data. The width of the lines indicates the tolerance range of 2 meV used to find matching values between the calculated series and PL spectrum. Supplementary Information reports a full description of this procedure. The good agreement between the PL spectra and calculated peak sequences generated using the energy values of the harmonics emerging from the N π^* orbitals suggests that most of the SPEs observed in the PL data have a common origin associated with the elementary excitation E_0 .

Although unable to offer a comprehensive understanding of the microscopic origin of SPEs in hBN, the DAP framework allows us to associate the elementary energy observed in RIXS with the single-photon emission process. Current theoretical approaches that aim to microscopically describe SPEs in hBN are mostly guided by the energy of ZPLs and phonon sidebands measured with PL spectroscopy^{8–11,48}. This often involves independently considering multiple SPEs, limiting the generality of the description, as we have proven that many SPEs are connected by an energy scale much lower than expected. Our evidence allows us to restrict the theoretical search for specific defects and highlights the importance of the p_z orbitals of nitrogen. Finally, we note that the similarities between the RIXS spectrum at the N π^* resonance of hBN and N₂ molecules could indicate a participation of N–N-like structures in the generation of SPEs^{32,33}. In this regard, theoretical calculations reported that nitrogen interstitial defects are incorporated

in hBN in a split-interstitial configuration and result in a structure similar to a N_2 molecule, introducing unoccupied gap states behaving as acceptors 48 . In the future, the use of wavefunction-based ab initio methods (that is coupled cluster single-double (CCSD), quantum chemistry) that consider the presence of harmonics states detected by RIXS and the involvement of N π^* orbitals will be fundamental for a deeper comprehension of quantum emission in hBN. Finally, we note that our findings do not exclude the presence of SPEs in hBN and fluorescent spin defects not related to harmonics at the N π^* resonance (such as the $V_{\rm R}^{-}$ defect 12,13).

Perspectives

In conclusion, by using RIXS in defective hBN, we uncover the elementary energy (E_0) of a harmonic series that spans from the mid-infrared to the ultraviolet, and correlates to SPEs observed in the PL spectra in the visible range. Due to the resonance selectivity of RIXS, we can pinpoint that N π^* bonds—rather than σ^* bonds—are active in the electronic transitions responsible for single-photon emission. Overall, our evidence describes a large number of phenomena reported in the literature, which are still under debate, and sets a solid basis for a complete description of SPEs in hBN. Finally, our work establishes RIXS as an important tool in the discovery and comprehension of low-dimensional photonic quantum materials.

Online content

Any methods, additional references, Nature Portfolio reporting summaries, source data, extended data, supplementary information, acknowledgements, peer review information; details of author contributions and competing interests; and statements of data and code availability are available at https://doi.org/10.1038/s41563-024-01866-4.

References

- Caldwell, J. D. et al. Photonics with hexagonal boron nitride. Nat. Rev. Mater. 4, 552–567 (2019).
- 2. Tran, T. T., Bray, K., Ford, M. J., Toth, M. & Aharonovich, I. Quantum emission from hexagonal boron nitride monolayers. *Nat. Nanotechnol.* **11**, 37–41 (2016).
- 3. Bourrellier, R. et al. Bright UV single photon emission at point defects in h-BN. *Nano Lett.* **16**, 4317–4321 (2016).
- Grosso, G. et al. Tunable and high-purity room temperature single-photon emission from atomic defects in hexagonal boron nitride. Nat. Commun. 8, 705 (2017).
- Fournier, C. et al. Position-controlled quantum emitters with reproducible emission wavelength in hexagonal boron nitride. Nat. Commun. 12, 3779 (2021).
- Dietrich, A. et al. Observation of Fourier transform limited lines in hexagonal boron nitride. *Phys. Rev. B* 98, 081414 (2018).
- Chejanovsky, N. et al. Single-spin resonance in a van der Waals embedded paramagnetic defect. Nat. Mater. 20, 1079–1084 (2021).
- 8. Jungwirth, N. R. & Fuchs, G. D. Optical absorption and emission mechanisms of single defects in hexagonal boron nitride. *Phys. Rev. Lett.* **119**, 057401 (2017).
- 9. Abdi, M., Chou, J.-P., Gali, A. & Plenio, M. B. Color centers in hexagonal boron nitride monolayers: a group theory and ab initio analysis. *ACS Photonics* **5**, 1967–1976 (2018).
- Tawfik, S. A. et al. First-principles investigation of quantum emission from hBN defects. Nanoscale 9, 13575–13582 (2017).
- Mendelson, N. et al. Identifying carbon as the source of visible single-photon emission from hexagonal boron nitride. *Nat. Mater.* 20, 321–328 (2021).
- Gottscholl, A. et al. Room temperature coherent control of spin defects in hexagonal boron nitride. Sci. Adv. 7, eabf3630 (2021).
- Gottscholl, A. et al. Initialization and read-out of intrinsic spin defects in a van der Waals crystal at room temperature. Nat. Mater. 19, 540–545 (2020).

- Tran, T. T. et al. Robust multicolor single photon emission from point defects in hexagonal boron nitride. ACS Nano 10, 7331–7338 (2016).
- Ament, L. J. P., van Veenendaal, M., Devereaux, T. P., Hill, J. P. & van den Brink, J. Resonant inelastic X-ray scattering studies of elementary excitations. Rev. Mod. Phys. 83, 705-767 (2011).
- Ament, L. J. P., van Veenendaal, M. & van den Brink, J. Determining the electron-phonon coupling strength from resonant inelastic X-ray scattering at transition metal L-edges. *Europhys. Lett.* 95, 27008 (2011).
- Gel'mukhanov, F., Odelius, M., Polyutov, S. P., Föhlisch, A. & Kimberg, V. Dynamics of resonant X-ray and Auger scattering. Rev. Mod. Phys. 93, 035001 (2021).
- Dvorak, J., Jarrige, I., Bisogni, V., Coburn, S. & Leonhardt, W. Towards 10 meV resolution: the design of an ultrahigh resolution soft X-ray RIXS spectrometer. Rev. Sci. Instrum. 87, 115109 (2016).
- Pelliciari, J. et al. Tuning spin excitations in magnetic films by confinement. Nat. Mater. 20, 188–193 (2021).
- 20. Pelliciari, J. et al. Evolution of spin excitations from bulk to monolayer FeSe. *Nat. Commun.* **12**, 3122 (2021).
- Dean, M. P. M. et al. Spin excitations in a single La₂CuO₄ layer. Nat. Mater. 11, 850–854 (2012).
- McDougall, N. L., Partridge, J. G., Nicholls, R. J., Russo, S. P. & McCulloch, D. G. Influence of point defects on the near edge structure of hexagonal boron nitride. *Phys. Rev. B* 96, 144106 (2017).
- Vinson, J., Jach, T., Müller, M., Unterumsberger, R. & Beckhoff, B. Resonant X-ray emission of hexagonal boron nitride. *Phys. Rev. B* 96, 205116 (2017).
- McDougall, N. L., Nicholls, R. J., Partridge, J. G. & McCulloch, D. G. The near edge structure of hexagonal boron nitride. *Microsc. Microanal.* 20, 1053–1059 (2014).
- Watanabe, K., Taniguchi, T. & Kanda, H. Direct-bandgap properties and evidence for ultraviolet lasing of hexagonal boron nitride single crystal. *Nat. Mater.* 3, 404–409 (2004).
- Xu, Z.-Q. et al. Single photon emission from plasma treated 2D hexagonal boron nitride. Nanoscale 10, 7957–7965 (2018).
- Serrano, J. et al. Vibrational properties of hexagonal boron nitride: inelastic X-ray scattering and ab initio calculations. *Phys. Rev. Lett.* 98, 095503 (2007).
- Geondzhian, A. & Gilmore, K. Demonstration of resonant inelastic X-ray scattering as a probe of exciton-phonon coupling. *Phys. Rev.* B 98, 214305 (2018).
- Geondzhian, A. & Gilmore, K. Generalization of the Franck-Condon model for phonon excitations by resonant inelastic X-ray scattering. *Phys. Rev. B* 101, 214307 (2020).
- Feng, X. et al. Disparate exciton-phonon couplings for zone-center and boundary phonons in solid-state graphite. *Phys. Rev. Lett.* 125, 116401 (2020).
- 31. Dashwood, C. et al. Probing electron-phonon interactions away from the Fermi level with resonant inelastic X-ray scattering. *Phys. Rev. X* 11, 041052 (2021).
- 32. Kjellsson, L. et al. Resonant inelastic X-ray scattering at the $N_2\pi^*$ resonance: lifetime-vibrational interference, radiative electron

- rearrangement, and wave-function imaging. *Phys. Rev. A* **103**, 022812 (2021).
- Lindblad, R. et al. X-ray absorption spectrum of the N₂⁺ molecular ion. Phys. Rev. Lett. 124, 203001 (2020).
- Ament, L. J., Van Veenendaal, M., Devereaux, T. P., Hill, J. P. & Van Den Brink, J. Resonant inelastic X-ray scattering studies of elementary excitations. Rev. Mod. Phys. 83, 705 (2011).
- Lee, J. et al. Charge-orbital-lattice coupling effects in the dd excitation profile of one-dimensional cuprates. Phys. Rev. B 89, 041104 (2014).
- Martinelli, L. et al. Collective nature of orbital excitations in layered cuprates in the absence of apical oxygens. *Phys. Rev. Lett.* 132, 066004 (2024).
- Comtet, J. et al. Wide-field spectral super-resolution mapping of optically active defects in hexagonal boron nitride. *Nano Lett.* 19, 2516–2523 (2019).
- 38. Hayee, F. et al. Revealing multiple classes of stable quantum emitters in hexagonal boron nitride with correlated optical and electron microscopy. *Nat. Mater.* **19**, 534–539 (2020).
- Mendelson, N. et al. Engineering and tuning of quantum emitters in few-layer hexagonal boron nitride. ACS Nano 13, 3132–3140 (2019).
- 40. Camphausen, R. et al. Observation of near-infrared sub-Poissonian photon emission in hexagonal boron nitride at room temperature. *APL Photonics* **5**, 076103 (2020).
- Schell, A. W., Svedendahl, M. & Quidant, R. Quantum emitters in hexagonal boron nitride have spectrally tunable quantum efficiency. Adv. Mater. 30, 1704237 (2018).
- 42. Grosso, G. et al. Low-temperature electron–phonon interaction of quantum emitters in hexagonal boron nitride. *ACS Photonics* **7**, 1410–1417 (2020).
- 43. Mendelson, N., Doherty, M., Toth, M., Aharonovich, I. & Tran, T. T. Strain-induced modification of the optical characteristics of quantum emitters in hexagonal boron nitride. *Adv. Mater.* **32**, 1908316 (2020).
- Nikolay, N. et al. Very large and reversible Stark-shift tuning of single emitters in layered hexagonal boron nitride. *Phys. Rev.* Appl. 11, 041001 (2019).
- 45. Williams, F. Donor-acceptor pairs in semiconductors. *Phys. Status Solidi B* **25**, 493–512 (1968).
- Tan, Q. et al. Donor-acceptor pair quantum emitters in hexagonal boron nitride. Nano Lett. 22, 1331–1337 (2022).
- Laturia, A., Van de Put, M. L. & Vandenberghe, W. G. Dielectric properties of hexagonal boron nitride and transition metal dichalcogenides: from monolayer to bulk. npj 2D Mater. Appl. 2, 6 (2018).
- 48. Weston, L., Wickramaratne, D., Mackoit, M., Alkauskas, A. & Van de Walle, C. Native point defects and impurities in hexagonal boron nitride. *Phys. Rev. B* **97**, 214104 (2018).

Publisher's note Springer Nature remains neutral with regard to jurisdictional claims in published maps and institutional affiliations.

This is a U.S. Government work and not under copyright protection in the US; foreign copyright protection may apply 2024

Methods

Growth and sample preparation

High-quality single-crystal hBN is grown under high pressure and high temperature²⁵. Flakes of different thicknesses are obtained by mechanical exfoliation on Si/SiO_2 substrates. Defects are induced in pristine samples by irradiation with argon plasma inside a reactive ion etcher at 25 W for 5 min, followed by annealing at 950 °C for 2 h in a tube furnace purged with nitrogen.

XAS and RIXS measurements

The XAS measurement at the N–K edge was performed at the 2-ID (SIX) beamline at NSLS-II, Brookhaven National Laboratory. The spectra were collected in the total electron yield and total fluorescence yield at 300 K, using vertically (σ) polarized light. The grazing-incidence angle is fixed at 30° for the XAS measurements. The X-ray beam size is 2 × 20 μ m² (V× H) and it is comparable with the flake size or smaller. Considering the size of the X-ray beam and the size of the flake, we can exclude any contribution from the edges of the samples.

RIXS measurements were performed at the 2-ID (SIX) beamline at NSLS-II, Brookhaven National Laboratory. All the samples are aligned with the surface normal (001) parallel to the scattering plane. The spectrometer arm is positioned at a fixed scattering angle of 90° . The incident light is σ polarized. The energy resolution is about 20 meV (full-width at half-maximum (FWHM)) at the N–K edge. All the measurements are performed at 300 K. Supplementary Information describes the fitting procedure. The X-ray beam size is $2\times20~\mu\text{m}^2~(V\times H)$ and it is comparable with the flake size or smaller. Considering the size of the X-ray beam and the size of the flake, we can exclude any contribution from the edges of the samples.

PL measurements

PL and spectroscopy measurements are performed in a home-built microscope setup coupled to a closed-cycle cryostat. An objective with a numerical aperture of 0.9 allows us to efficiently collect emission from areas with a diameter of 1.5 μ m. Experiments are performed in a reflection geometry by exciting the sample with either a continuous-wave green laser (532 nm) or a supercontinuum pulsed laser with a tunable filter having a bandwidth of 2 nm. The laser reflection is removed from the PL signal by long-pass filters. The spectra are measured by a spectrometer with a high-resolution grating (1,200 gratings per mm) and an electron-multiplying charge-coupled device camera. Second-order correlation functions $g^{(2)}(\tau)$ are measured in a Hanbury Brown and Twiss instrument with free-space-coupled avalanche photodiodes and by filtering individual spectral lines using tunable long- and short-pass filters.

Data availability

Relevant data are available from the corresponding authors upon reasonable request.

Code availability

The DAP analysis code is available from the corresponding authors upon reasonable request.

Acknowledgements

We thank A. Gali for fruitful discussions. Work at Brookhaven National Laboratory was supported by the US Department of Energy (DOE) Office of Science under contract no. DE-SC0012704 (J.P., Y.G., J.L., S.F. and V.B.). This work was also supported by the Laboratory Directed Research and Development project of Brookhaven National Laboratory No. 21-037 (J.P. and S.F.) and by the US DOE Office of Science, Early Career Research Program (V.B. and Y.G). This research used Beamline 2-ID of the National Synchrotron Light Source II, a US DOE Office of Science User Facility, operated for the DOE Office of Science by Brookhaven National Laboratory under contract no. DE-SC0012704. Work at CUNY is supported by the National Science Foundation (NSF) (grant no. DMR-2044281) (G.G.), the physics department of the Graduate Center of CUNY and the Advanced Science Research Center (E.M., J.M.W., S.B.C. and G.G.) and the Research Foundation through PSC-CUNY award no. 64510-00 52 (G.G.). K.W. and T.T. acknowledge support from the Elemental Strategy Initiative conducted by MEXT, Japan (grant no. JPMXP0112101001), and JSPS KAKENHI (grant nos. 19H05790, 20H00354 and 21H05233).

Author contributions

J.P. and G.G. conceived the project. J.P., Y.G., J.L., S.F. and V.B. performed the RIXS experiments. T.T. and K.W. synthesized the high-quality hBN. E.M. and G.G. developed the material process to generate the defective hBN. E.M. prepared the pristine and highly defective hBN samples. E.M. performed the PL experiments with the help of J.M.W., S.B.C. and G.G. E.M., J.M.W. and G.G. developed the fitting methods. J.P. and G.G. wrote the manuscript with input from all authors.

Competing interests

The authors declare no competing interests.

Additional information

Supplementary information The online version contains supplementary material available at https://doi.org/10.1038/s41563-024-01866-4.

Correspondence and requests for materials should be addressed to Jonathan Pelliciari or Gabriele Grosso.

Peer review information *Nature Materials* thanks Jeroen van den Brink and the other, anonymous, reviewer(s) for their contribution to the peer review of this work.

Reprints and permissions information is available at www.nature.com/reprints.